Supporting Information

In-vivo fast non-linear microscopy reveals impairment of fast axonal transport induced by molecular motor imbalances in the brain of zebrafish larvae

Baptiste Grimaud,[†,#] Maxence Frétaud,[‡,¶,#] Feriel Terras,[†,#] Antoine Bénassy,[†] Karine Duroure,[§] Valérie Bercier,[‖] Gaëlle Trippé-Allard,[†] Rabei Mohammedi,[⊥] Thierry Gacoin,[⊥] Filippo Del Bene,[§] François Marquier,[†] Christelle Langevin,[*,‡] and François Treussart[*,†]

†*Université Paris-Saclay, ENS Paris-Saclay, CNRS, CentraleSupélec, LuMIn, 91190 Gif-sur-Yvette, France*

‡*Université Paris-Saclay, INRAE, IERP, 78350 Jouy-ens-Josas, France*

¶*Université Paris-Saclay, INRAE, VIM, 78350 Jouy-en-Josas, France*

§*Sorbonne Université, INSERM, CNRS, Institut de la Vision, 75012 Paris, France*

‖*VIB, Center for Brain and Disease Research, Laboratory of Neurobiology, 3000 Leuven, Belgium*

⊥*Laboratory of Condensed Matter Physics, Ecole Polytechnique, CNRS, Institut Polytechnique de Paris, 91128 Palaiseau cedex, France*

#*These authors equally contributed to the work*

E-mail: christelle.langevin@inrae.fr; francois.treussart@ens-paris-saclay.fr

1. Supporting data

S1. NanoKTP electron microscopy images and size distribution

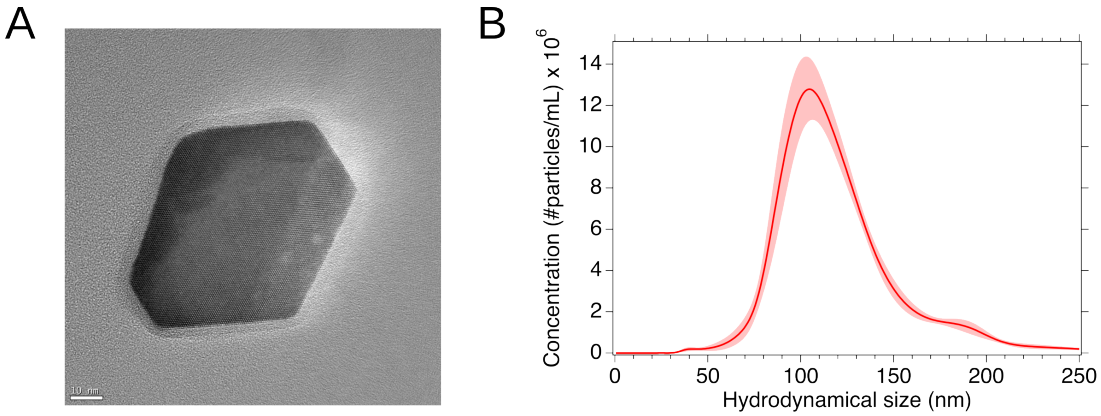

Figure S1: NanoKTP characterization.(A) High resolution transmission electron microscopy image in bright field, acquired with a JEOL JEM-2010F (operated at 200 kV voltage) aberration corrected (Cs: 1.4 mm and Cc: 1.0 mm). The nominal magnification is 400,000 (the effective one on the array detector is 522,049), and the image is acquired -60 nm under-focus. Scale bar: 10 nm. (B) NanoKTP hydrodynamical size distribution as measured by nanoparticle tracking analysis. Red shaded area indicates the limits of five consecutive measurements and the solid line is the average of them.

We used a nanoparticle tracking analysis device (NanoSight NS300, Malvern Panalytical, UK) to measure the hydrodynamical diameter distribution of the size-selected nanoKTP solution (Supporting Figure S1B). We repeated the measurement five times, and the average mean value is 123.8 ± 2.4 nm (standard deviation over the 5 measurements indicated) and an average mode position of 104.0 ± 2.7 nm. To estimate the width of the averaged distribution we fitted it with a Gaussian (not shown) and obtained a standard deviation of 21 nm.

S2. Emitted light spectrum

Taking advantage of the prism-based spectrum resolution capability of the Leica SP8 microscope we used, we measured the spectrum of the light emitted from a single nanoKTP excited with the pulsed laser (Chameleon Ultra II, Coherent Inc.) set at the 1040 nm wavelength and observed a peak (Figure S2) which FWHM of 10 nm corresponds to a Fourier transform-limited spectral width of 160 fs. This pulse duration value is in good agreement with the laser specifications of 140 fs, considering the dispersion-induced pulse duration broadening (due in particular to the microscope objective), that is not fully compensated by the pre-compensation module installed between the laser output and the microscope. Moreover, the emission spectrum is perfectly centered on 520 nm, half of the excitation wavelength of 1040 nm. Both the pulse width and duration values confirm that we detect the second-harmonic generation light from nanoKTP.

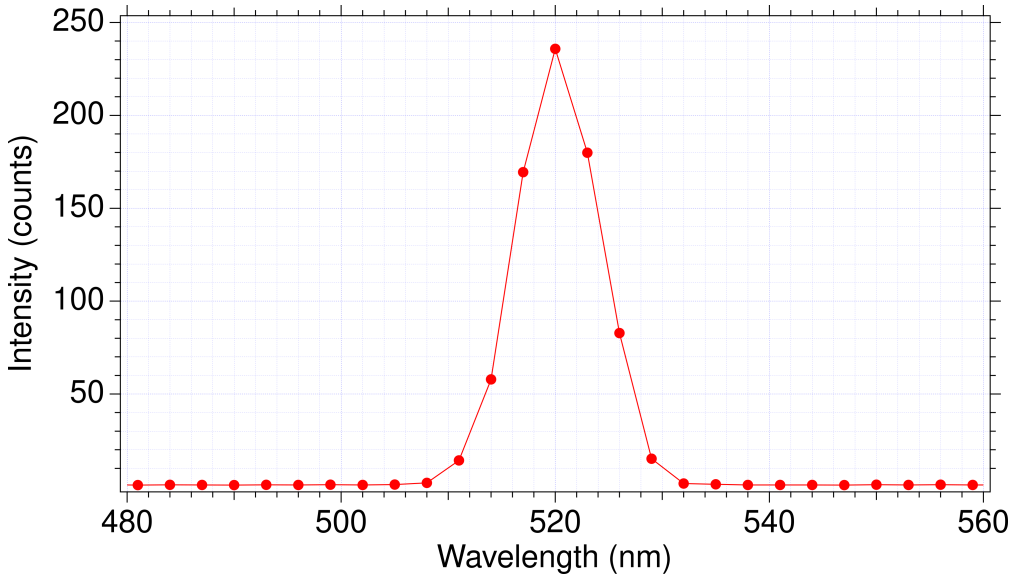

Figure S2: Spectrum of the emitted light from a single nanoKTP as recorded with "lambda scan" mode of the Leica SP8 microscope, showing a narrow band centered on 520 nm corresponding to a SHG signal.

S3. Conversion of 8 bits-encoded hybrid detector intensity levels in photon counts

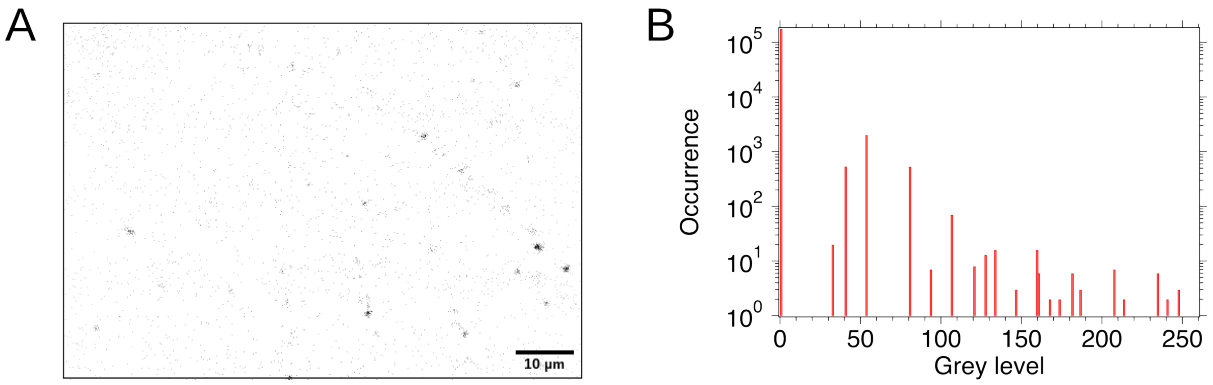

Figure S3: Estimate of the conversion of grey level into numbers of detected photons by the HyD used in the "standard mode". (A) Frame #665 of Supporting Video S1. (B) Histogram of grey levels present in (A) in logarithmic scale, displaying 21 peaks between the dominant white 0 level (excluded from count) associated to zero detected photons and 255 (black) maximum possible level. The maximum grey level present in (A) is 247.

We estimated the conversion factor between photon counts to 8 bits-encoded intensity grey level from the histogram of grey levels in the whole frame #665 of the Supporting Video S1 considering that each additional intensity peak results from the counting of one more photon. The maximum intensity peak is the 21st one, and corresponds to a value of 247. Assuming, as a crude approximation, a linear dependence, the photon-to-intensity

conversion factor is $K_{\text{conv}} \approx 247/21 \approx 11.8$ photons per gray level. Let us point out that we have assumed an increment of 1 photon between two consecutive peaks, but it could be larger. Hence, this value of K_{conv} is an upper bound. However, the selection of the frame #665 was motivated by two reasons: 1) fact that its largest grey level value of 247 is close to the saturated maximum (255) but lower than it, and 2) because it displays the largest number of peaks of the whole frames. This careful selection should reduce the discrepancy between the estimated conversion factor and the ground truth one.

S4. Precision of localization of the nanoKTP: theoretical estimate and comparison with its measurement

We determined the theoretical precision of localization of a single nanoKTP from the number of photons detected during the raster scan of its SHG emission. This limit is defined as the Cramèr-Rao bound (CRB) (σ_{CRB}, being the standard deviation) from Fisher information theory. As the photons constituting SHG spot are collected pixel after pixel along the raster scan and not at once on the pixels of an array detector (as in Single Molecule Localization Microscopies, SMLM), different theoretical limits can be achieved for the two acquisition methods[1]. However, it can be shown in the case where we only take into account the photon shot noise[2] that for a Gaussian shape excitation beam (which is a very good approximation of the focused excitation laser spot), both the SMLM and raster-scanning imaging modes yield almost the same lower bound[3]: $\sigma_{\text{CRB}} = s/\sqrt{N}$, where s is the PSF standard deviation, and N the total number of photons detected over the spot.

We estimated s from one of the brightest SHG spots associated to a nanoKTP immobilized on a glass microscope coverslip. We extracted such spot, displayed on Supporting Figure S4A, from Supporting Video S3 which is one of the seven one-minute duration videos of SHG signal from immobile nanoKTP we recorded. As the nanoparticle has a non negligible size relative to the expected s value, the SHG spot intensity distribution results from the convolution of the particle profile (approximated to a sphere of diameter $d^{\text{nanoKTP}} = 120$ nm) and the PSF_{exp} function. Figure S4A shows one of the brightest spots and Gaussian fits of two orthogonal centered cross-sections with standard deviations $s_x^{\text{nanoKTP}} = 304$ nm and $s_y^{\text{nanoKTP}} \approx 363$ nm. As a crude approximation: $s \approx (s_x^{\text{nanoKTP}} + s_y^{\text{nanoKTP}})/2 - d^{\text{nanoKTP}} \approx 215$ nm. By integrating the grey levels of intensity of all pixel composing Supporting Figure S4A spot, and using the conversion factor determined in section S3, we obtain $N_{\text{avg}} = 439$, leading to $\sigma_{\text{CRB}}^{\text{min}} = 215/\sqrt{484} \approx 10$ nm.

The experimental value we measured for this spot is the standard deviation of the Gaussian fit center positions in consecutive frame of the video (Supporting Figure S4B), which is $\sigma_{xy} \approx 50$ nm. This value appears to be larger than the theoretical estimate $\sigma_{\text{CRB}}^{\text{min}}$, probably due to mechanical vibrations. We then considered other spots of different intensities from all the seven videos. Figure S4C displays the variation of σ_{xy} with the integrated photon counts per spot.

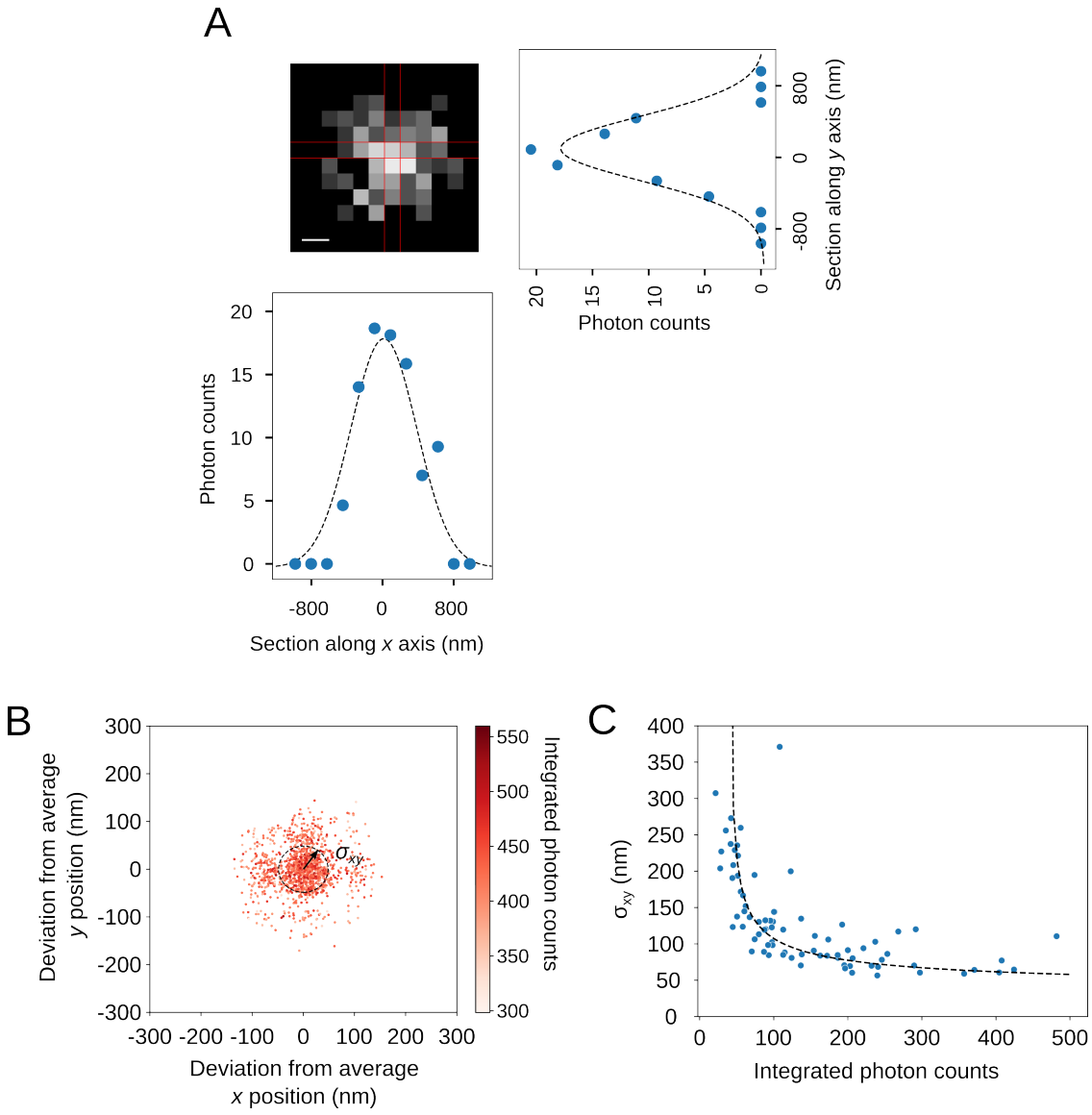

Figure S4: Measurement of the imaging precision of localization. (A) SHG spot from one nanoKTP immobilized on a glass coverslip. Bottom and right are intensity sections along lines $y = 0$ and $x = O$ respectively, blue points being the experimental values and the dashes black lines being Gaussian fits. (B) Scatter plot of Gaussian fit center position of the same spot than in (A) in consecutive frames of Supporting Video S3. σ_{xy} arrow and dashed line circle represents the standard deviation of the distribution of positions centered on the average one. (C) Distribution of σ_{xy} for an ensemble of SHG spots of different mean integrated photon counts. The dashed black line is the empirical function $30+600/\sqrt{N-40}$ in nanometers (N being the integrated photon counts), serving as a guide for the eyes.

S5. Confinement ratio threshold to parse the trajectory in Go and Stop phases

The confinement ratio R_i is determined at each point i along all the trajectories over a duration of $6\Delta t = 0.3$ s ($\Delta t = 50$ ms being the duration of one full frame scan), corresponding

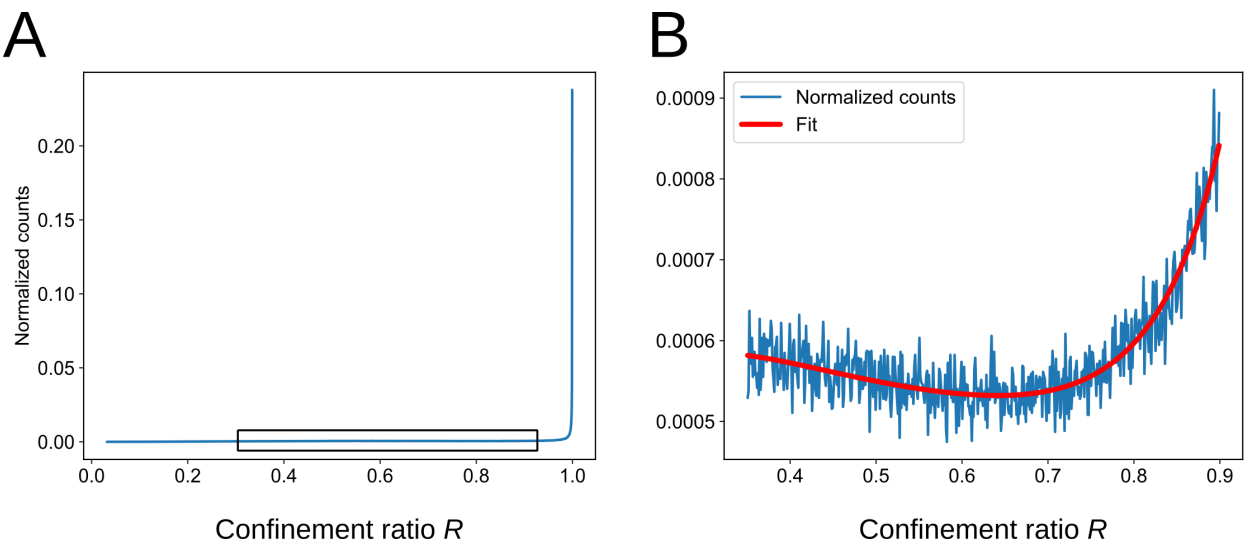

Figure S5: Determination of the confinement ratio threshold R_{th} to parse the trajectories in Go and Stop phases of motion. (A) Histogram of the confinement ratio values for all trajectories of all conditions of *kif5aa* larvae. The black rectangle defines the region where we can observe a minimum of R. (B) Zoom on the black rectangle region: the minimum $R_{\text{th}} = 0.64$ is obtained from a polynomial fit (red line) of the histogram (blue line).

to 3 preceding plus 3 successive measured positions of the nanoparticle. A unit value corresponds to a perfectly directional motion, whereas a zero value means that the particle came back at the exact same location after a duration of $6\Delta t$. The histogram of $\{R_i\}$ is shown on Supporting Figure 5. To analyze the intraneuronal transport from our experiment, we separate the globally directional motions from the more diffusive ones, characterized by lower confinement ratio values. We find a threshold between these two behaviors by representing the logarithmic counts as a function of R and isolating a local minimum using a 5^{th}-order polynomial fit. The minimum is found for $R_{\text{th}} \approx 0.64$, which is the threshold used to parse each trajectory in Stop and Go phases.

S6. Absence of effect of nanoKTP on lysosomes axonal transport

To evaluate the potential impact of nanoKTP injection on axonal transport, we labeled lysosomes with LysoTracker live dye, traced their motion at the same frame rate (20 fps) than nanoKTP and extracted their transport parameters with the same analysis pipeline as the one used for nanoKTP. The extraction of trajectories was not as efficient for LysoTracker positive vesicle than for nanoKTP, due to a lower signal-to-background ratio, as can be seen in Fig. S7. However, we collected enough data in the different conditions and Figure S6 shows that lysosomes (LysoTracker-labeled vesicles) axonal transport parameters are not altered by nanoKTP injection.

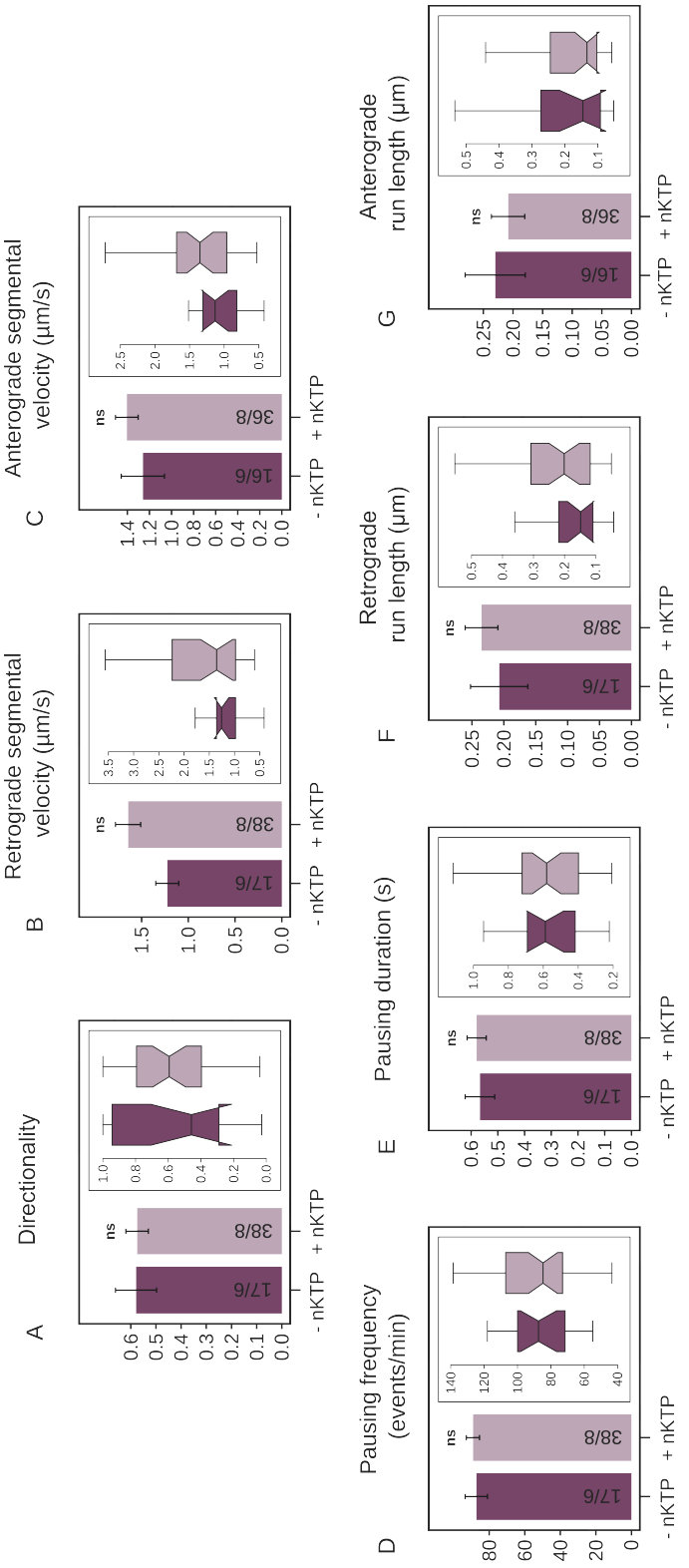

Figure S6: Effects of nanoKTP on lysosome axonal transport parameters. (Continued on the following page)

Figure S 6: We bathed Zf larvae at 4 dpf with LysoTracker Red to trace lysosomes and compared two conditions: with nanoKTP (+nKTP) injected at 3 dpf or without (-nKTP). Lysosome transport parameters were extracted with the same analysis pipeline as nanoKTP. As a reminder, the directionality (A) is the cumulative length of retrograde segment divided by the total length of the trajectory. (B) and (C) are the retrograde and anterograde segmental velocities, respectively. (D) and (E) are the pausing frequency and pausing duration respectively, while (F) and (G) are the anterograde and retrograde runlengths, respectively. None of these parameters present significant differences between +nKTP and -nKTP conditions (from (A) to (G): $p = 0.87$, 0.15, 0.18, 0.78, 0.85, 0.31 and 0.97). Numbers in the bars are # trajectories/# of animals.

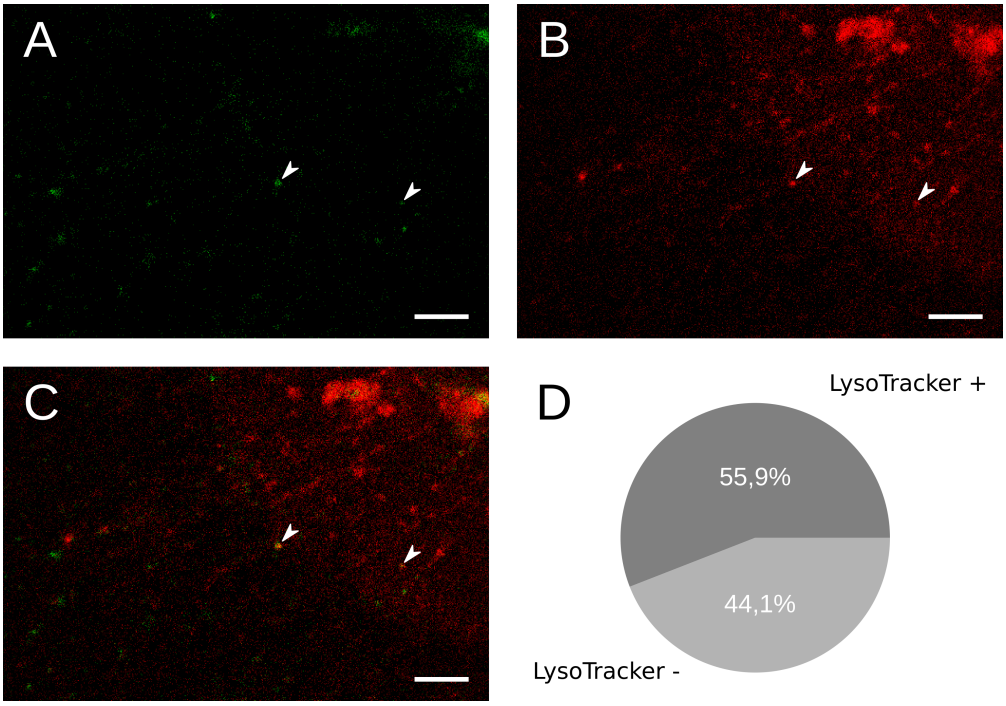

Figure S7: Colocalization of mobile nanoKTP with lysosomes. (A) One frame of the green channel (nanoKTP) of a two-color (green and red, see Materials and Methods) video. (B) LysoTracker Red channel of the exact same frame. (C) Merge of green and red channels. The two arrow heads point towards nanoKTP having directed motions and colocalizing with LysoTracker Red positive compartment. (D) Result of the mobile nanoKTP-LysoTracker colocalization analysis from one experiment carried out for on 8 larvae, 62 fields of views (from both brain sides), leading to a total of 38 nanoKTP trajectories. LysoTracker +/- correspond respectively to nanoKTP containing vesicles that are positive/negative to LysoTracker signal. Scale bars: 10 µm.

S7. Colocalization of nanoKTP with lysosomes

Considering that we inject the nanoKTP 24h before imaging, we anticipate that after their endocytosis, they are most likely located in late endosomes and lysosomes. To check this

hypothesis, we conducted an additional experiment in which the nanoKTP injected larvae were bathed with LysoTracker Red live imaging dye, and then imaged in two-color channels (green for nanoKTP, red for LysoTracker) at 20 fps. We only focused on mobile nanoKTP (with directed motion), which are the only one for which we can ascertain the uptake. Figure S7(A-C) displays an example of a field-of-view with two mobile nanoKTP colocalizing with LysoTracker Red vesicles. Fig. S7D is the statistical summary, concluding to about 56% of the nanoKTP in late endosomes or lysosomes.

S8. Reversal of directionality quantification for dynapyrazole-treated larvae and *kif5aa* larvae.

The directional switch frequency, displayed on Figure S8 in the case of dynapyrazole treatment and for *kif5aa* larvae, is calculated as the number of events where a Go phase of a given direction is followed by a Go phase of the opposite direction, after a Stop. The number of events was then normalized by the duration in seconds of the trajectory.

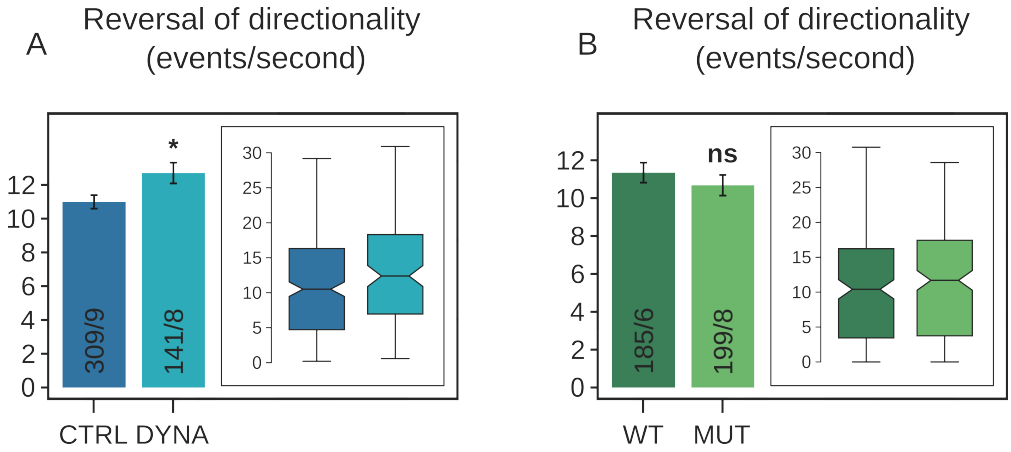

Figure S8: Directional switch frequency in the case of dynapyrazole treatment (A) and for *kif5aa* larvae (B). Dynapyrazole increases the switch frequency from to ($p = 0.025$). There is no switch frequency difference between WT and MUT *kif5aa* ($p = 0.352$)). Numbers in the bars are # trajectories/# of animals

S9. Separate quantification of pausing duration for pauses between two anterograde or two retrograde phases of motion, or between phases of opposite directions

The separate quantification of pausing duration displayed in Figure S9 excludes, by construction, pauses at the extremities of trajectories.

S10. Collection efficiency of SHG light emitted by a single monocrystalline nanoKTP

The geometry and notations are defined in the Supporting Figure S10A.

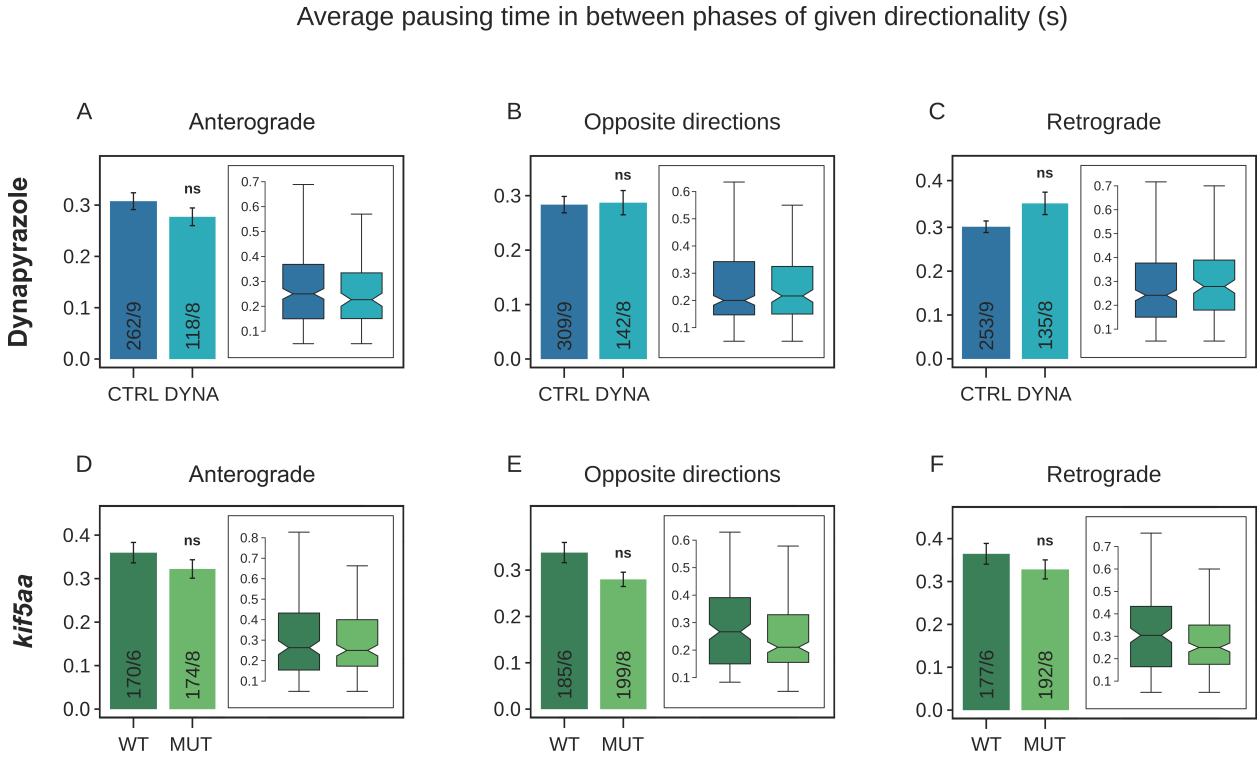

Figure S9: Average pausing durations between phases of motion of given directionality, in the case of DYNA (A-C) and *kif5aa* (D-F) experiments. Pausing duration between two anterograde phases (A,D), two retrograde phases (C,F) or two phases of opposite direction of motion (B,E). p-values are, from A to F, respectively: 0.57, 0.67, 0.09, 0.58, 0.16 and 0.21. Numbers in the bars are # trajectories/# of animals.

As $d_{33} = 16.9$ pm/V nonlinear coefficient of KTP dominates the others (ranging from 1.9 to 4.3 pm/V), we consider the SHG emission as solely due to an induced dipole $\mathbf{p}_3$ along the nanocrystal c-axis $\mathbf{u}_3$:

$$\mathbf{p}_3(\theta, \varphi) = 2\varepsilon_0 d_{33} |E_3(\theta, \varphi)|^2 \mathbf{u}_3,$$

where $E_3(\theta, \varphi)$ is the projection of the circularly polarized excitation laser electric field $\mathbf{E}^{\text{inc}}$ on $\mathbf{u}_3$. In the following we will consider $\varphi = 0$ ($\mathbf{e}_x$ along the direction of the projection of $\mathbf{p}_3$ in the sample plane (Oxy)), without any restriction of generality due to the cylindrical symmetry along the microscope objective axis (Oz), so that $\mathbf{u}_3 = \sin\theta \mathbf{e}_x + \cos\theta \mathbf{e}_z$, with θ being the polar orientation angle of $\mathbf{p}_3$ relative to (Oz)

The SHG total collected power $P_{2\omega}(\theta)$ (where ω is the pulsation of the excitation laser) results from the angular integration of all Poynting vectors of electromagnetic fields at 2ω pulsation, with unitary vector directions $\mathbf{u} = \sin\theta' \cos\varphi' \mathbf{e_x} + \sin\theta' \sin\varphi' \mathbf{e_y} + \cos\theta' \mathbf{e_z}$.

We first consider the radiated power per unit solid angle of collection around $\mathbf{u}$, which is known to have the form:

$$\frac{dP_{2\omega}}{d\Omega} = K |\mathbf{p}_{3\perp}(\theta)|^2, \tag{1}$$

where K is a constant, and $\mathbf{p}_{3\perp} \equiv \mathbf{p}_3 - (\mathbf{p}_3.\mathbf{u})\mathbf{u}$ is the the projection of $\mathbf{p}_3$ in the plane perpendicular to $\mathbf{u}$.

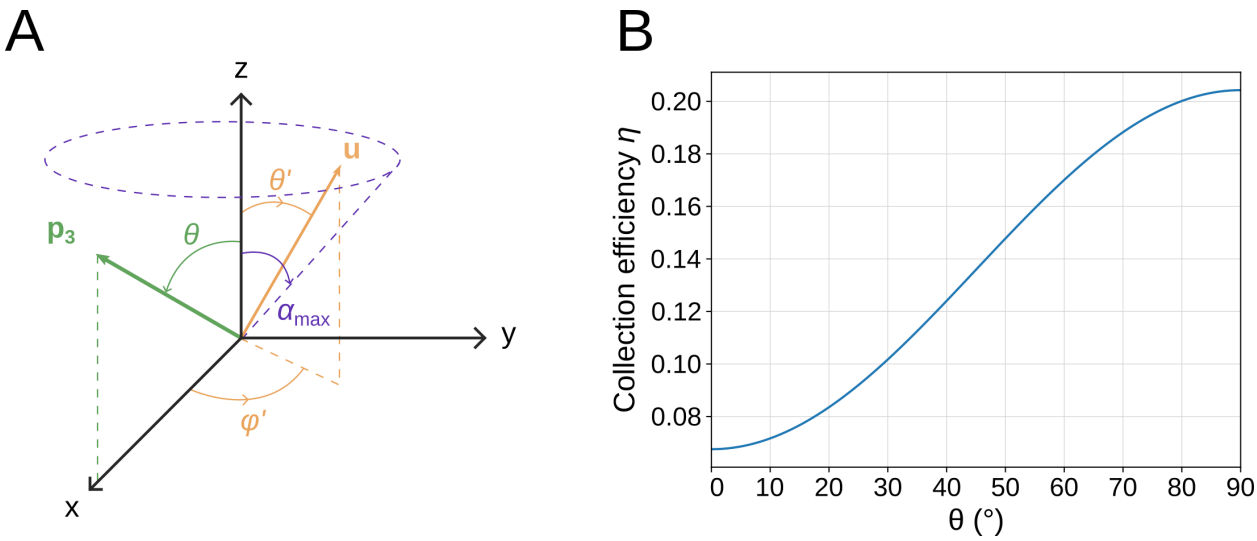

Figure S10: Collection efficiency of the SHG signal from a single nanoKTP. (A) Geometry for the calculation of the collection efficiency. The SHG is excited with a pulsed laser beam focused in the sample plane orthogonal to the microscope objective symmetry axis (Oz). The excitation light is circularly polarized to ensure equal excitation of nanoKTP with different crystalline axis orientations. We model the nanocrystal second-order nonlinear response as the one of a dipole $\mathbf{p}_3$ (along the crystal c-axis). For a given nanocrystal, we can select the (Ox) axis to match the projection of this dipole in the sample plane, with no loss of generality. SHG emission is collected through the same objective. $\mathbf{u}$ denotes one unitary vector direction of SHG wave vector, with dircetion defined by φ' and θ' angles. θ' ranges between 0 and $\alpha_{\max}$, defined through $NA = n_{\mathrm{w}} \sin \alpha_{\max}$, with $NA = 0.95$, the numerical aperture of the microscope objective, and $n_{\mathrm{w}} = 1.3$ the index of refraction of the aqueous imaging medium. In our case $\alpha_{\max} \approx 50.3°$. (B) SHG collection efficiency $\eta(\theta)$ of a nanoKTP as a function of its polar orientation θ, with respect to the microscope objective axis (Oz). $\eta(\theta)$ varies as $\sin^2 \theta$ with a contrast depending on the numerical aperture NA. Plot drawn for water immersion microscope objective with $NA = 0.95$.

One can show that $|\mathbf{p}_{3\perp}|^2 = |\mathbf{p}_3|^2 M(\theta, \theta', \varphi')$, where:

$$M(\theta, \theta', \varphi') = 1 - \left(\sin^2\theta \sin^2\theta' \cos^2\varphi' + \cos^2\theta \cos^2\theta' + \frac{1}{2} \sin 2\theta \sin 2\theta' \cos\varphi' \right)$$

Hence, $P_{2\omega}(\theta)$ is obtained by integrating equation (1) over the solid angles $d\Omega$, with the upper limit $\alpha_{\max}$ of integration on θ' defined by the numerical aperture NA of the microscope objective ($NA = n_{\mathrm{w}} \sin \alpha_{\max}$, where $n_{\mathrm{w}} = 1.3$ is the index of refraction of water):

$$\begin{aligned} P_{2\omega}(\theta) &= |\mathbf{p}_3|^2 \int_0^{\alpha_{\max}} \left(\int_0^{2\pi} M(\theta, \theta', \varphi') d\varphi' \right) \sin\theta' d\theta' \\ &= |\mathbf{p}_3|^2 \left[\pi \cos\alpha_{\max} \sin^2\alpha_{\max} \sin^2\theta + \frac{2\pi}{3} \left(2 + \cos^3\alpha_{\max} - 3\cos\alpha_{\max} \right) \right] \\ &= |\mathbf{p_3}|^2 A(\theta, \alpha_{\max}), \end{aligned}$$

where the notation $A(\theta, \alpha_{\max}) \equiv B(\alpha_{\max}) \sin^2\theta + C(\alpha_{\max})$ is introduced to clarify the expression.

Of note, integrating on 4π steradian results in $A_{4\pi} = \frac{8\pi}{3}$. The power $P_{2\omega}(\theta)$ can thus be normalized by this value, leading to the collection efficiency $\eta(\theta)$:

$$\eta(\theta) \equiv \frac{P_{2\omega}(\theta)}{|\mathbf{p}_3|^2 A_{4\pi}} = \frac{3}{8\pi}[B(\alpha_{\max}) \sin^2\theta + C(\alpha_{\max})] \tag{2}$$

Supporting Figure S10B displays $\eta(\theta)$.

S11. Example of $\theta(t)$ retrieval from SHG intensity variation. Case of static nanoKTP.

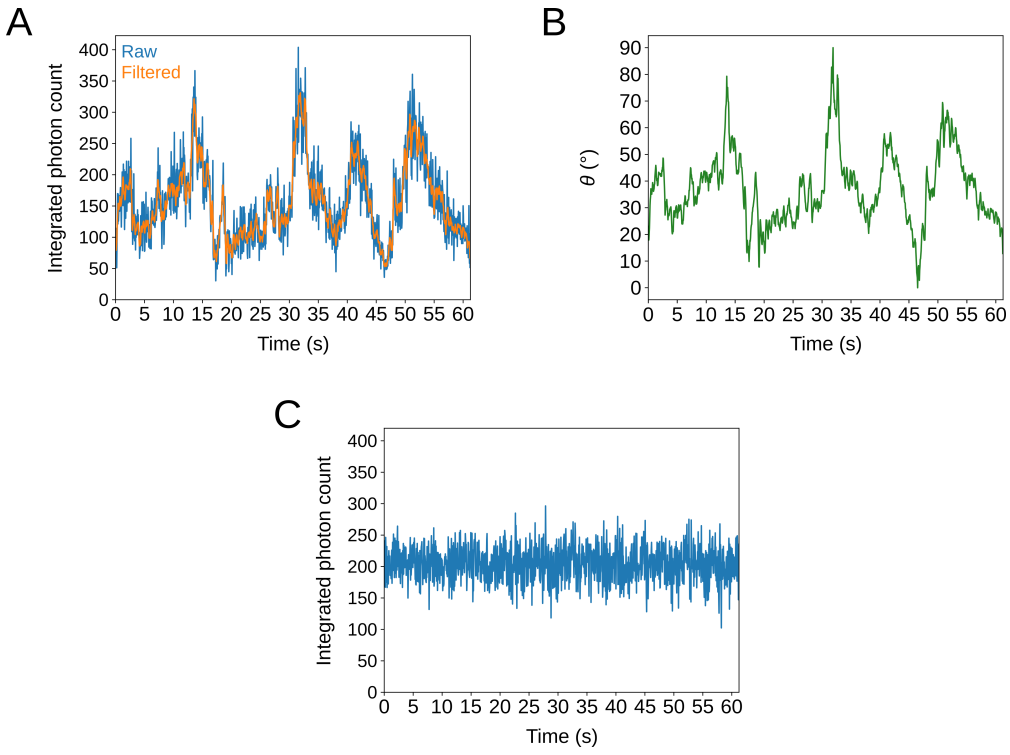

Figure S11: SHG detected intensity $I_{2\omega}(t)$ variation of one mobile and one static nanoKTP, and $\theta(t)$ inference. (A) SHG intensity time trace from a nanoKTP following a directed motion (inset) in an axon of HOM *kif5aa* larva. The blue trace is the raw data with 50 ms time interval between consecutive frames. The orange superimposed trace results from filtering the raw trace with a Savitzky-Golay filter using a sliding window of 11 time intervals and a third order polynomial fit. (B) $\theta(t)$ time trace inferred from (A) $I_{2\omega}(t)$ using equation (3), assuming that $I_{2\omega}$ minimum and maximum correspond respectively to 0° and 90°. (C) Intensity fluctuations of a static nanoKTP immobilized on a glass microscope coverslip. Intensity is expressed in photon counts as estimated from the conversion detailed in Supporting Data S3.

Supporting Figure S6 shows an example of $\theta(t)$ retrieval from a nanoKTP with a directed motion. We assumed that the detected SHG intensity (in unit of extrapolated photon counts per frame duration) $I_{2\omega}^{\min}$ and $I_{2\omega}^{\max}$ are reached for $\theta = 0°$ and $90°$ respectively, so that $\theta(t)$ is retrieved, in radians, by:

$$\theta(t) = \arcsin \sqrt{\frac{I_{2\omega}(t) - I_{2\omega}^{\min}}{I_{2\omega}^{\max} - I_{2\omega}^{\min}}} \tag{3}$$

In order to reduce the sensitivity of $\theta(t)$ retrieval to SHG intensity large but short fluctuations, we applied a Savitzky-Golay filter to $I_{2\omega}(t)$ of all trajectories (orange curve in Fig. S11A) prior to the extraction of $\theta(t)$ (Fig. S11B) by equation 3. Fig. S11C displays the SHG intensity time trace of one of the immobilized nanoKTP used to determined the localization precision (Fig. S4). As our method to retrieve θ angular variations cannot be applied to a static particle, we cannot convert the intensity fluctuation into angular fluctuations for static particles. However, we believe that $I_{2\omega}(t)$ fluctuations mainly result from mechanical vibrations resulting in slight change of focus and excitation intensity in the sample plane. Indeed, the average intensity and standard deviation for the static particle considered are respectively $\overline{I_{2\omega}} = 205.0$ and $\sigma_I = 26.8$ counts (per time frame), while the shot-noise limit for $\sigma_{I_{2\omega}}^{\mathrm{SN}} = \sqrt{\overline{I_{2\omega}}} = 14.7$. The excess of noise is consitent with our localisation precision not limited by the shot-noise, but rather by mechanical vibrations (Fig. S4C).

S12. Fluctuations of orientations of nanoKTP-labeled endolysosomal vesicle in dynapyrazole-treated zebrafish larvae

Supporting Figure S12 displays the standard deviation σ_θ quantifying the fluctuation of polar angle θ for larvae treated by DYNA compared to untreated control, in Go and Stop phases.

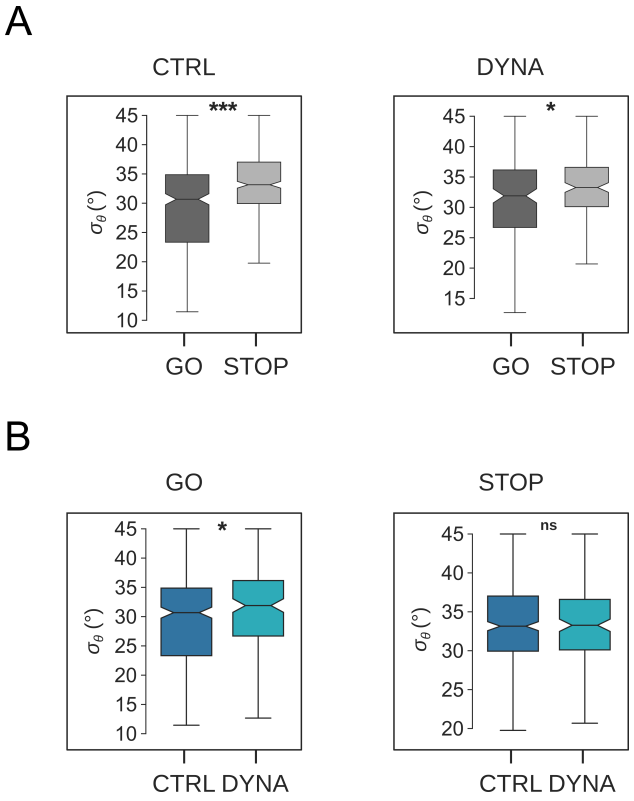

Figure S12: Fluctuation of orientation σ_θ of nanoKTP-labeled vesicle during the Go and Stop phases of motion in neurons of the brain of Zf larvae treated with dynapyrazole-A, compared to controlled untreated ones. As reported for *kif5aa* larvae (Figure 5), σ_θ is larger in the Stop phases of motion than in the Go ones for both Control (increase of 8%) and DYNA conditions (increase of 8.0%), $p = 2.2 \times 10^{-12}$ and 0.02 respectively. Comparing σ_θ between different conditions for each phase of motion, we observe that DYNA treatment induces an increase of 4.8%, from 29.3° to 30.7° in average, of σ_θ in the case of the Go phases ($p = 0.03$) but not in the Stop phases ($p = 0.44$).

2. Supporting videos

Supporting Video S1 is the raster-scanning video from which Fig. 2A was calculated, showing in inverted grey scale the SHG signal of nanoKTP moving in PVN neuron of a zebrafish larva (*kif5aa* wild-type). True frame rate of 20 frames/s, total of 2354 frames. Scale bar: 10 μm. Supporting Video S2 is another raster-scanning video showing in inverted grey scale the SHG signal of nanoKTP moving in PVN neuron of a hetegozygous *kif5aa* zebrafish larva. True frame rate of 20 frames/s, total of 2501 frames. Scale bar: 10 μm. Supporting Video S3 displays SHG of individual nanoKTP drop-casted on a glass coverslip, that was used to infer the precision of localization displayed on Supporting Figure S4, with 10 other similar videos. They all were acquired in the exact same conditions as the videos of nanoKTP directed motion in the ZF larvae brain, *i.e.* in particular at 20 frame/s, inside the thermally controlled cage incubator.

References

1. Balzarotti, F.; Eilers, Y.; Gwosch, K. C.; Gynnå, A. H.; Westphal, V.; Stefani, F. D.; Elf, J.; Hell, S. W. Nanometer resolution imaging and tracking of fluorescent molecules with minimal photon fluxes. Science **2017**, 355, 606–612.

2. Masullo, L. A.; Lopez, L. F.; Stefani, F. D. A common framework for single-molecule localization using sequential structured illumination. Biophysical Reports **2022**, 2, 100036.

3. Deschout, H.; Zanacchi, F. C.; Mlodzianoski, M.; Diaspro, A.; Bewersdorf, J.; Hess, S. T.; Braeckmans, K. Precisely and accurately localizing single emitters in fluorescence microscopy. Nature Methods **2014**, 11, 253–266.